Supporting Information for:

In vivo microrheology reveals local elastic and plastic responses inside three-dimensional bacterial biofilms

Authors:
Takuya Ohmura[1], Dominic J. Skinner[2,3], Konstantin Neuhaus[1,4], Gary P. T. Choi[5], Jörn Dunkel[2,*], Knut Drescher[1,*]

Affiliations:
[1]Biozentrum, University of Basel, Spitalstrasse 41, Basel, 4056, Switzerland
[2]Department of Mathematics, Massachusetts Institute of Technology, 77 Massachusetts Avenue, Cambridge, MA, 02139-4307, USA
[3]NSF-Simons Center for Quantitative Biology, Northwestern University, Evanston, IL, 60201, USA
[4]Department of Physics, Philipps-Universität Marburg, Renthof 5, Marburg, 35032, Germany
[5]Department of Mathematics, The Chinese University of Hong Kong, N.T., Hong Kong
[#]Correspondence: dunkel@mit.edu, knut.drescher@unibas.ch

Contents:

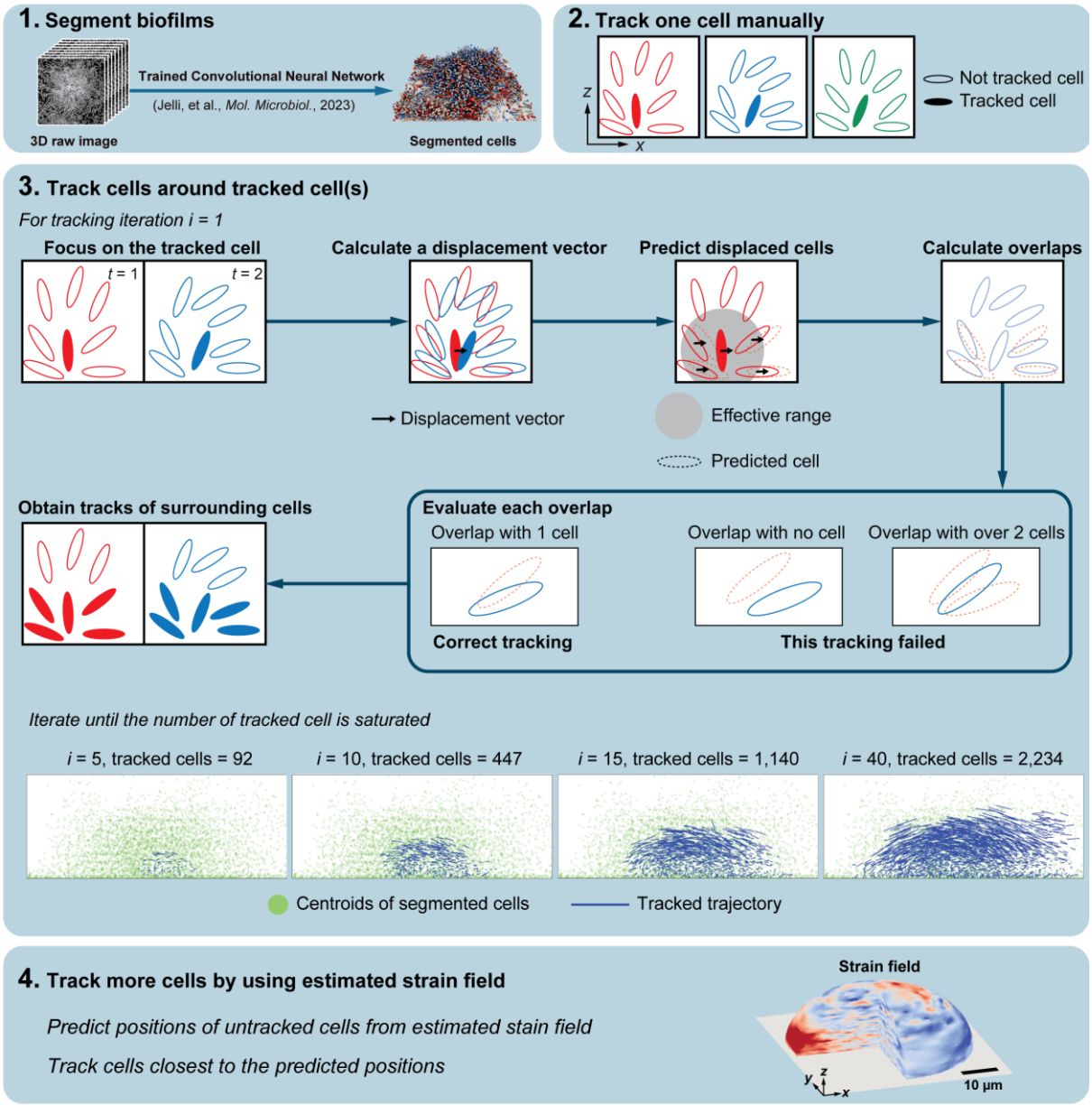

Figure S1: Iterative cell tracking algorithm for large cell displacements.
Workflow employed for cell tracking during biofilm deformation under strong shear flow and recovery after return to baseline flow. Step (1): Segmentation cell labels are obtained from raw 3D images by using the pre-trained neural network that is part of the StarDist OPP method. Cell tracking requires high-accuracy of cell segmentation. Step (2): Looking at cells close to the substrate surface in the biofilm from the bottom view, a human annotator can easily track at least one cell between three time points (Before, Deformed, After). Step (3): In every tracking iteration i + 1, all tracked cells in the previous iteration i are checked for tracking overlap. Bottom plots show the tracked cells at different iterations i, on the xz-plane during deformation at shear rate $\dot{\gamma}$ = 8.16 x 10^4 s^{-1}. As the iteration index i increases, positions of successfully tracked cells propagate from the bottom center toward outer boundary of the biofilm. Step (4): The tracking iteration in Step (3) assumes that the displacement magnitude of cells inside a biofilm is a continuous variable. Therefore, cells which are displaced with a longer distance than their neighbor, or cells which are far from neighboring cells cannot be tracked in the Step (3).

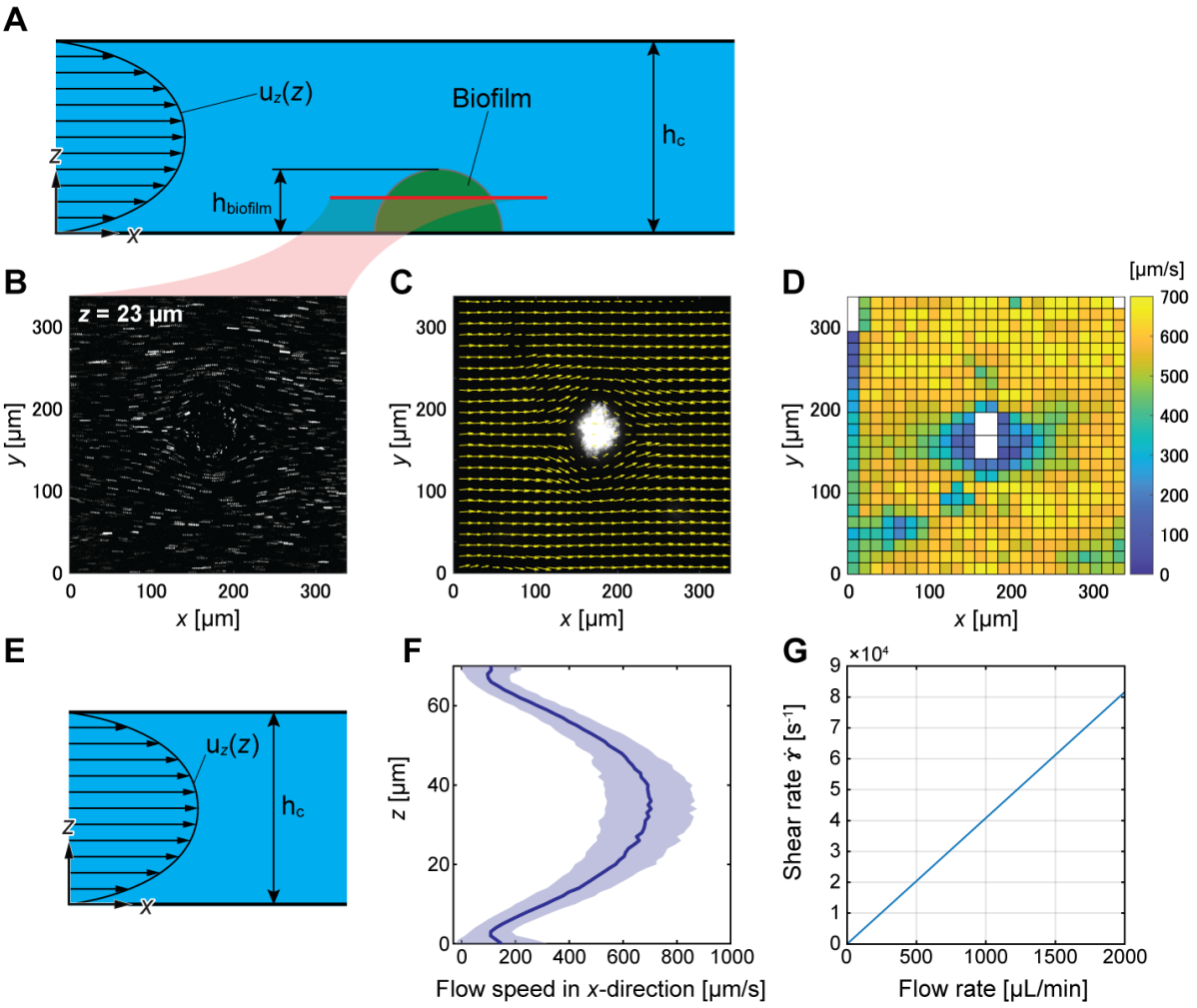

Figure S2: Flow profile around a biofilm in a microchannel.
A) Schematic diagram of the expected flow profile in the *xz*-plane in a microchannel. The flow in our rectangular microchannel is expected to be laminar and parabolic along the *z*-axis. Biofilms grow on the glass surface located at $z = 0$ µm. Images are acquired with a confocal microscope at a particular *z*-plane, indicated by a red line. B) Visualization of flowing fluorescent beads (diameter = 0.1 µm) in the *xy*-plane around a biofilm at $z = 23$ µm (exposure time = 15 ms, flow rate = 1.0 µl/min). C) Flow field vectors calculated from the image in panel B (and replica images acquired at the same position), plotted on top of an image of the biofilm at $z = 23$ µm. Yellow arrows indicate flow magnitude and direction. The biofilm is located in the center of image. The flow field indicates laminar flow, and the flow field is symmetric around the biofilm in the *y*-axis and in the *x*-axis, which is consistent with fluid dynamics at low Reynolds number. D) Flow speed in the *xy*-plane around the biofilm at $z = 23$ µm, at the same location as in panels B, C. E) Schematic diagram of the expected flow profile in a microfluidic channel without biofilms. F) Experimentally measured flow speed along the *x*-direction in the microfluidic channel without a biofilm, as a function of *z*-height in the channel. While the flow close to the walls was not detected correctly, the flow profile > 5 µm away from the walls was parabolic, consistent with fluid mechanics theory. G) Relationship between flow rate, which is an experimentally controlled parameter, and shear rate $\dot{\gamma}$ at the bottom of the microfluidic channel without biofilms.

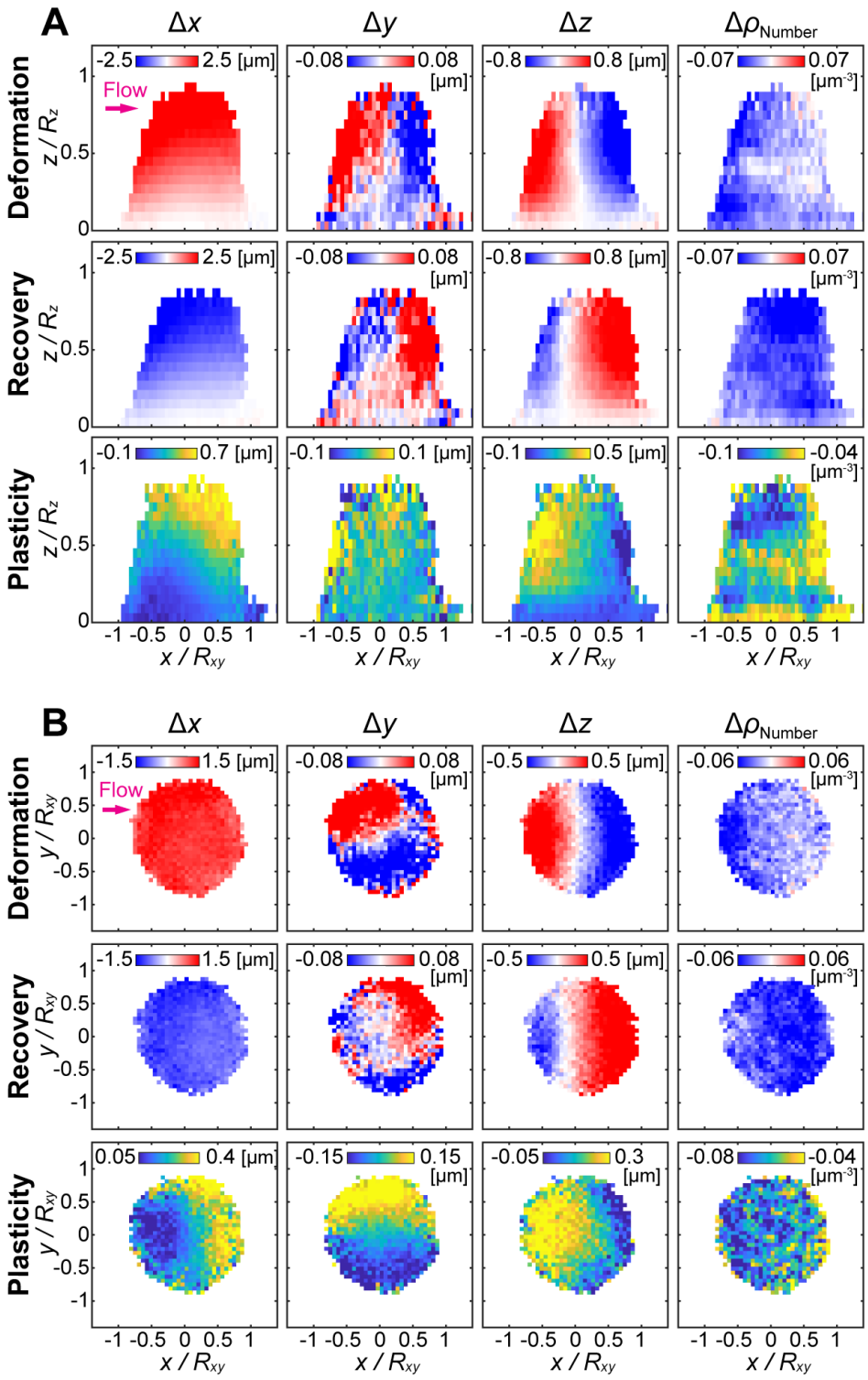

Figure S3: Spatial profiles of changes in additional single-cell parameters, in biofilms exposed to a large change in fluid shear rate.

Spatial distribution of single-cell-level parameters: Δx, Δy, Δz are displacements of cells in *x*-axis, *y*-axis, *z*-axis, respectively, and $\Delta\rho_{\mathrm{Number}}$ is the change of cell number density around a cell. Changes are computed for the Deformation, Recovery, or Plasticity, as defined in Fig. 1A. Data are averaged for biofilms exposed to a shear rate $\dot{\gamma} = 8.16 \times 10^4\ s^{-1}$, for flow duration times = 20 min and 40 min, and for biofilm volumes $V > 2{,}800\ \mu m^3$ (corresponding to data for $n = 13$ independent biofilms). A) Data are shown on the *xz*-plane. B) Data are shown on the *xy*-plane.

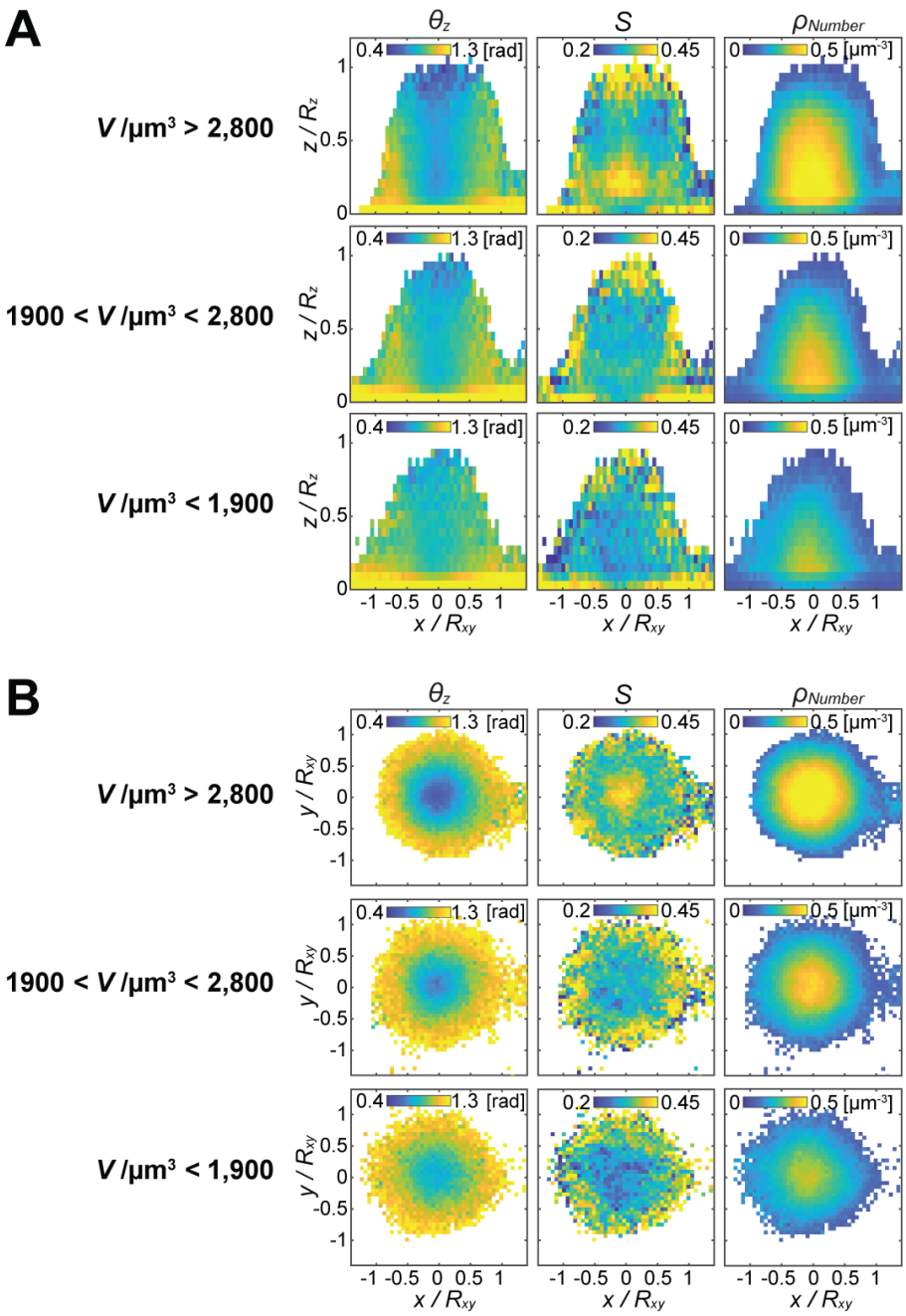

Figure S4: Spatial profiles of single-cell parameters in biofilms with different volumes, before the increase in fluid shear rate.

A) Spatial distributions of three single-cell parameters (θ_z, S, ρ_{Number}) before the shear-rate-increase, shown in the *xz*-plane. Each row of heatmaps represents a particular range of biofilm volume: Large biofilms (V > 2,800 µm^3), mid-sized biofilms (1,900 µm^3 < *V* < 2,800 µm^3), and small biofilms (V < 1,900 µm^3). The data is averaged for *n* = 40 biofilms for the large biofilms, *n* = 44 biofilms for the mid-sized biofilms and *n* = 58 biofilms for the small biofilms. B) Spatial distributions of the single-cell parameters before the shear-rate-increase in the *xy*-plane.

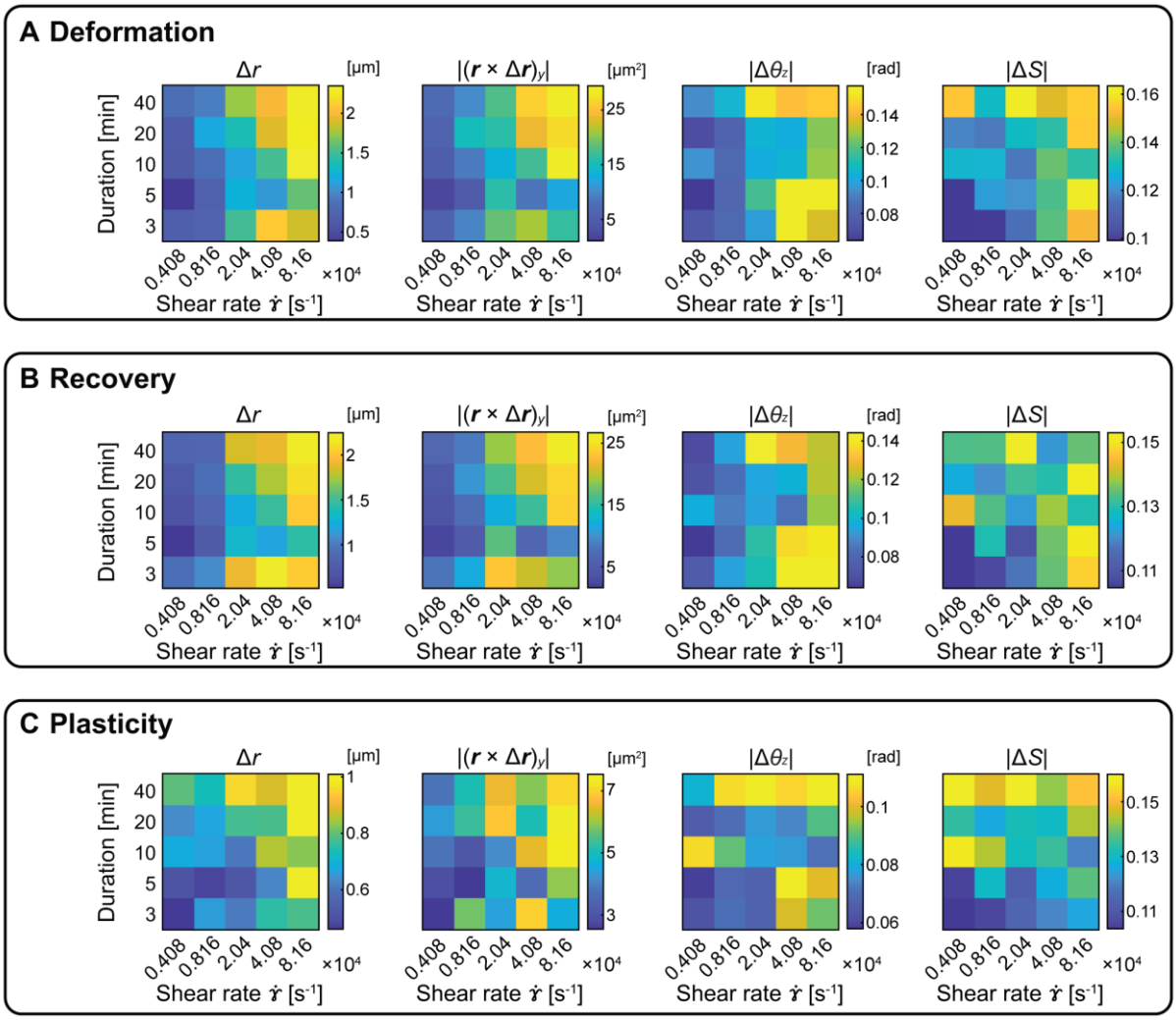

Figure S5: Phase diagrams showing changes of biofilm architecture parameters caused by changes in shear flow: Effects of shear rate magnitude and duration of exposure to high shear rate.
A) Biofilm architecture changes during deformation. Each heatmap shows the effect of the maximum shear rate and the duration of the exposure to the maximum shear rate on changes of the biofilm architecture parameters (Δr, cell displacement; $|(\boldsymbol{r} \times \Delta \boldsymbol{r})_y|$, angular-momentum-like displacement cross-product; $|\Delta\theta_z|$, change in cell alignment with the *z*-axis; $|\Delta S|$, change in local nematic order). Each pixel within a heatmap is the average value for all cells in all biofilms in this condition. B) Biofilm architecture changes during recovery (after reducing the shear rate from the maximum back to 0 s^{-1}). C) Biofilm architecture changes characterizing plasticity.

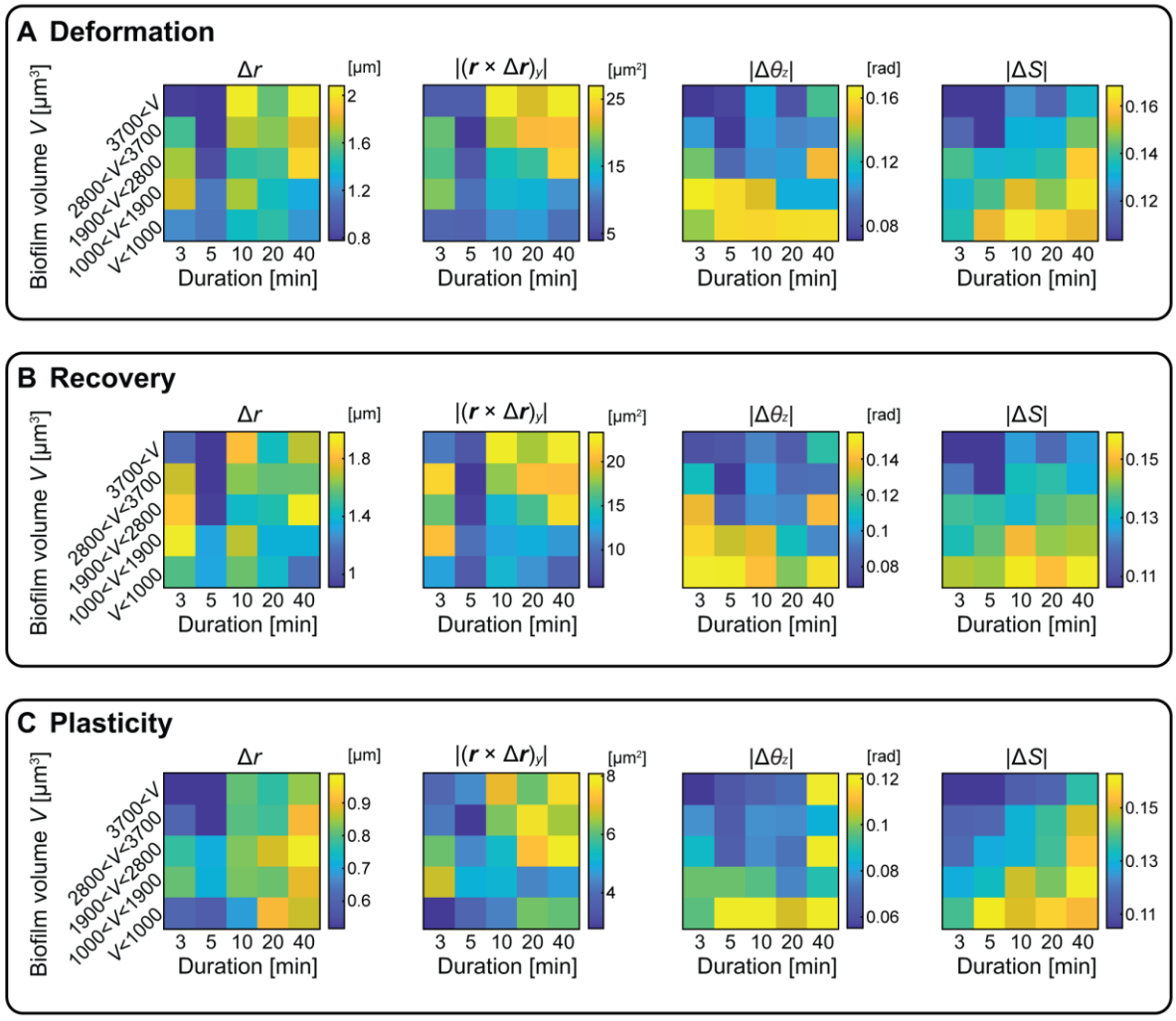

Figure S6: Phase diagrams showing changes of biofilm architecture parameters caused by changes in shear flow: Effects of the biofilm volume and duration of exposure to high shear rate.

A) Biofilm architecture changes during deformation. Each heatmap shows the effect of the biofilm volume *V* and the duration of the exposure to the maximum shear rate on changes of the biofilm architecture parameters (Δr, cell displacement; $|(\boldsymbol{r} \times \Delta \boldsymbol{r})_y|$, angular-momentum-like displacement cross-product; $|\Delta\theta_z|$, change in cell alignment with the *z*-axis; $|\Delta S|$, change in local nematic order). Each pixel within a heatmap is the average value for all cells in all biofilms in this condition. B) Biofilm architecture changes during recovery (after reducing the shear rate from the maximum back to 0 s^{-1}). C) Biofilm architecture changes characterizing plasticity.

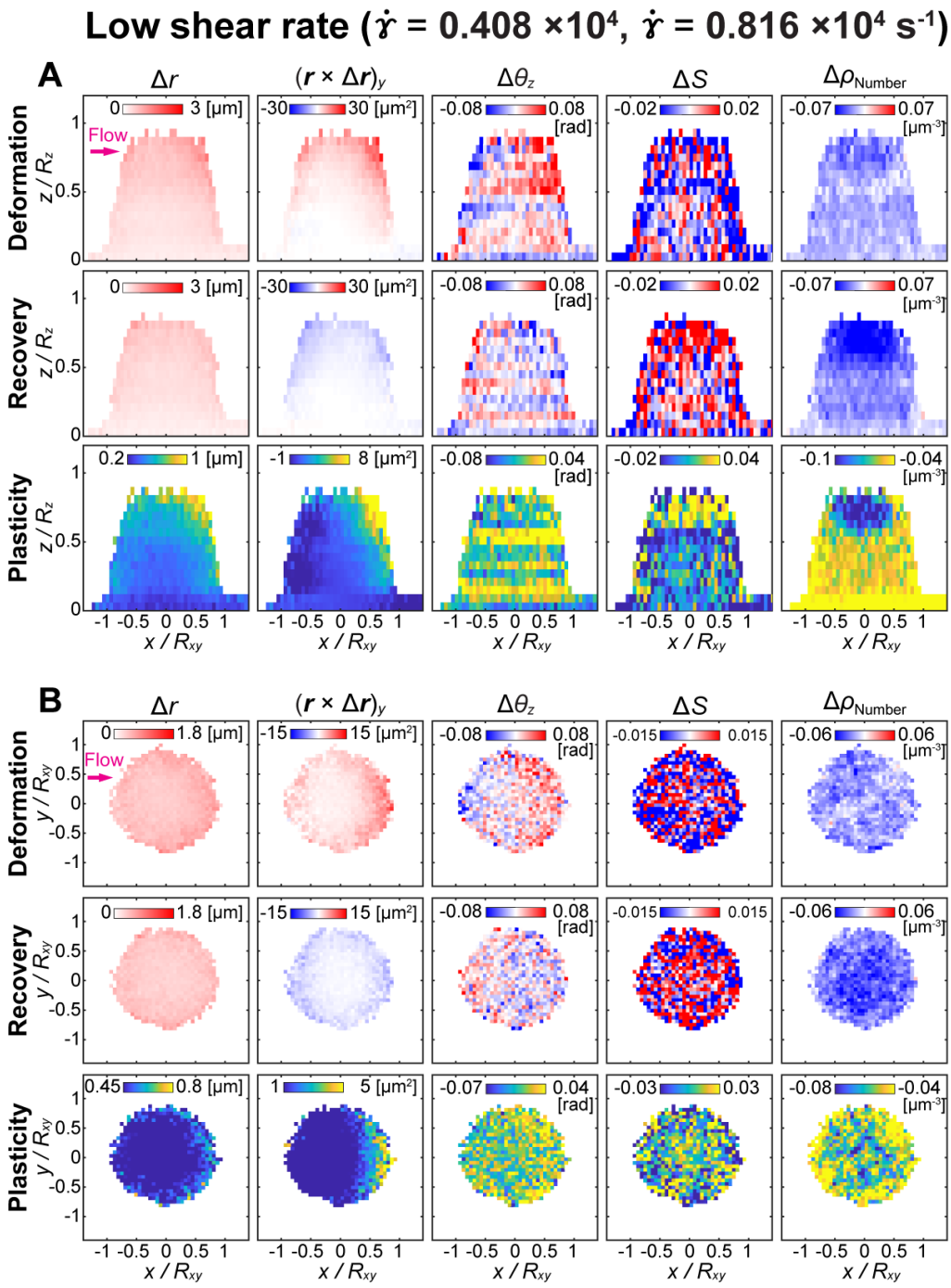

Figure S7: Spatial profiles of changes in single-cell parameters, in biofilms exposed to changes in shear flow with low amplitude.

Spatial distribution of changes in five single-cell parameters (Δr, $(\boldsymbol{r} \times \Delta \boldsymbol{r})_y$, $\Delta\theta_z$, ΔS, $\Delta\rho_{\mathrm{Number}}$) for biofilms exposed to relatively low amplitudes of shear-rate-increases: from $\dot{\gamma} = 0$ s^{-1} to $\dot{\gamma} = 0.408$ x 10^4 s^{-1} or 0.816 x 10^4 s^{-1}. Data from n = 13 independent biofilms with V > 2,800 μm³ and for experiments with 20 min and 40 min duration of exposure to high shear rates were averaged. Each row of heatmaps shows the five single-cell parameters for a particular condition: Deformation, Recovery, and Plasticity, which are terms that are defined in Fig. 1A. A) Spatial distributions in the *xz*-plane. B) Spatial distributions in the *xy*-plane. Compared with the changes of single-cell parameters caused by exposure to a high shear rate (Fig. 2, Fig. S3), the changes in single-cell-level parameters following exposure to low shear rates are substantially smaller.

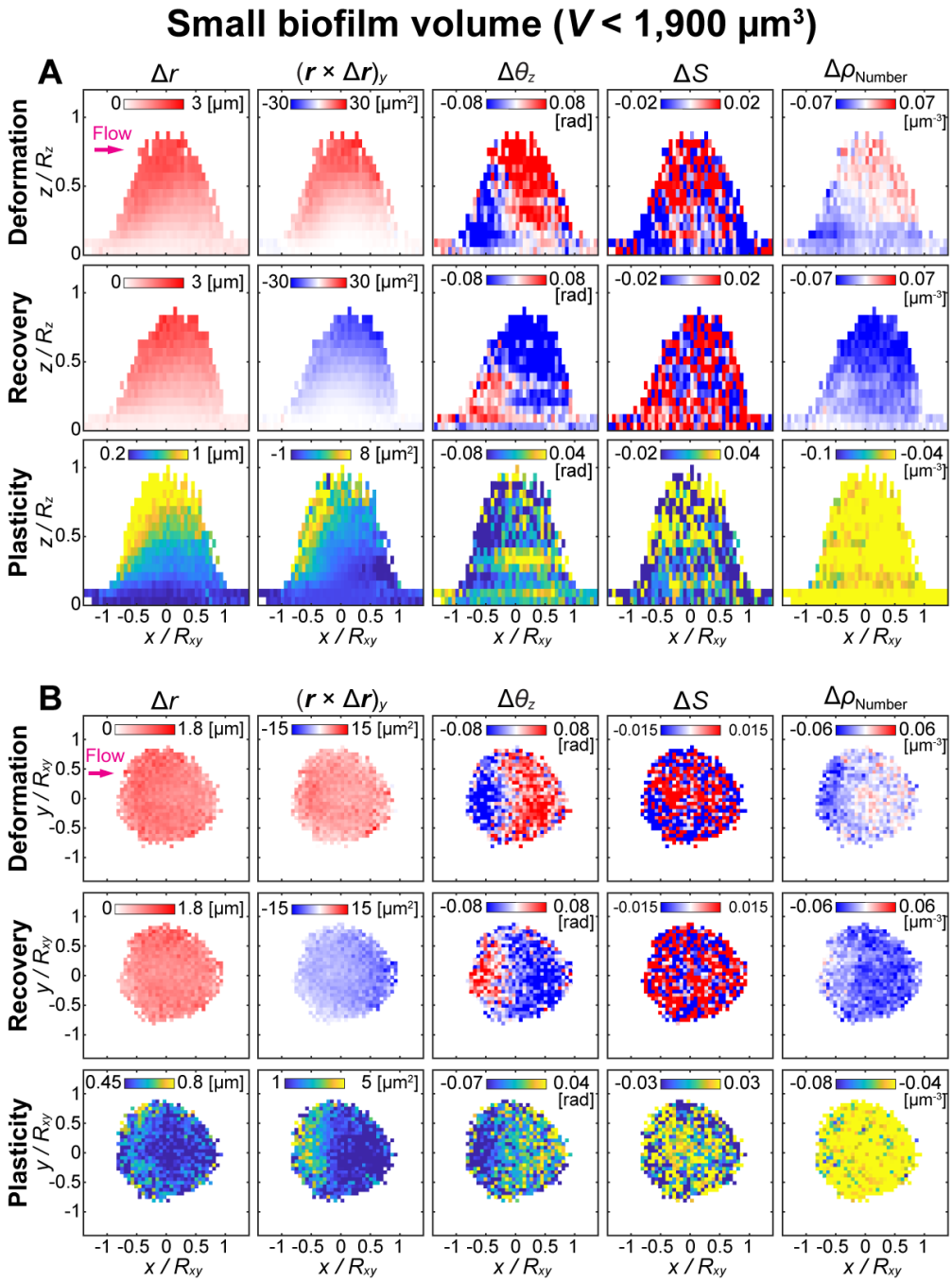

Figure S8: Spatial profiles of changes in single-cell parameters, in small biofilms exposed to changes in shear flow.

Spatial distribution of changes in five single-cell parameters (Δr, $(\boldsymbol{r} \times \Delta \boldsymbol{r})_y$, $\Delta\theta_z$, ΔS, $\Delta\rho_{\mathrm{Number}}$) for relatively small biofilms (V < 1,900 µm^3) exposed to strong fluid shear ($\dot{\gamma} = 8.16 \times 10^4$ s^{-1}) for a duration of 20 or 40 min. Data from *n* = 20 independent biofilms were averaged. Each row of heatmaps shows the five single-cell parameters for a particular condition: Deformation, Recovery, and Plasticity, which are terms that are defined in Fig. 1A. A) Spatial distributions in the *xz*-plane. B) Spatial distributions in the *xy*-plane. Compared with the changes in single-cell-level parameters for larger biofilms (Fig. 2, Fig. S3), the displacements at the front of the biofilm are larger than at the rear.

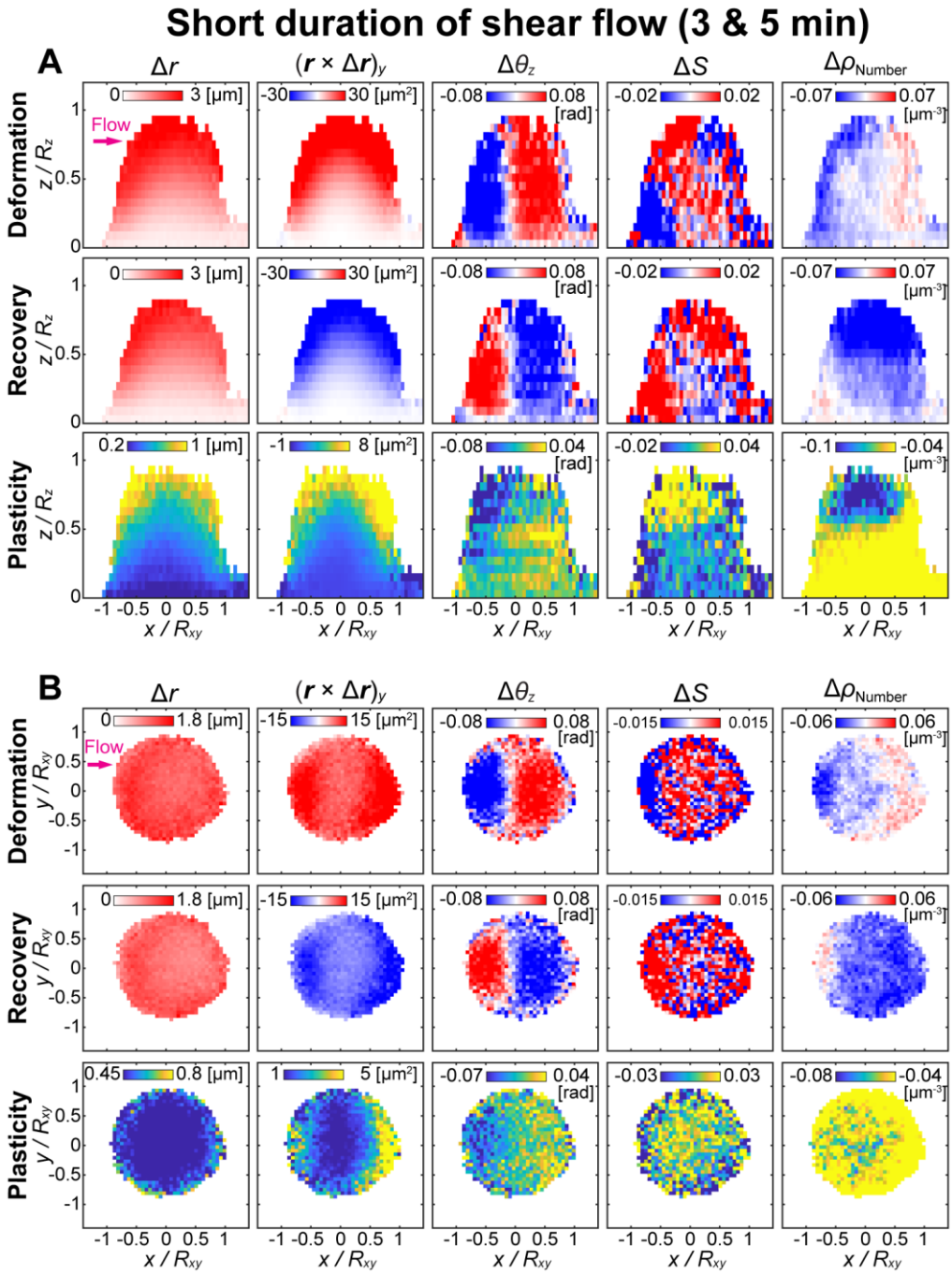

Figure S9: Spatial profiles of changes in single-cell parameters, in biofilms exposed to short durations of flow with high shear rate.

Spatial distribution of changes in five single-cell parameters (Δr, $(\boldsymbol{r} \times \Delta \boldsymbol{r})_y$, $\Delta\theta_z$, ΔS, $\Delta\rho_{\mathrm{Number}}$) for biofilms exposed to strong shear flow for a relatively short duration (3 or 5 mins). Data from n = 16 independent biofilms with V > 2,800 µm^3 and for experiments with shear rate $\dot{\gamma} = 8.16 \times 10^4$ s^{-1} were averaged. Each row of heatmaps shows the five single-cell parameters for a particular condition: Deformation, Recovery, and Plasticity, which are terms that are defined in Fig. 1A. A) Spatial distributions in the *xz*-plane. B) Spatial distributions in the *xy*-plane. Compared with the single-cell-level parameter distributions that are observed for a longer duration of exposure to shear flow (Fig. 2, Fig. S3), the changes in Plasticity are smaller, but the changes in Deformation and Recovery are similar.

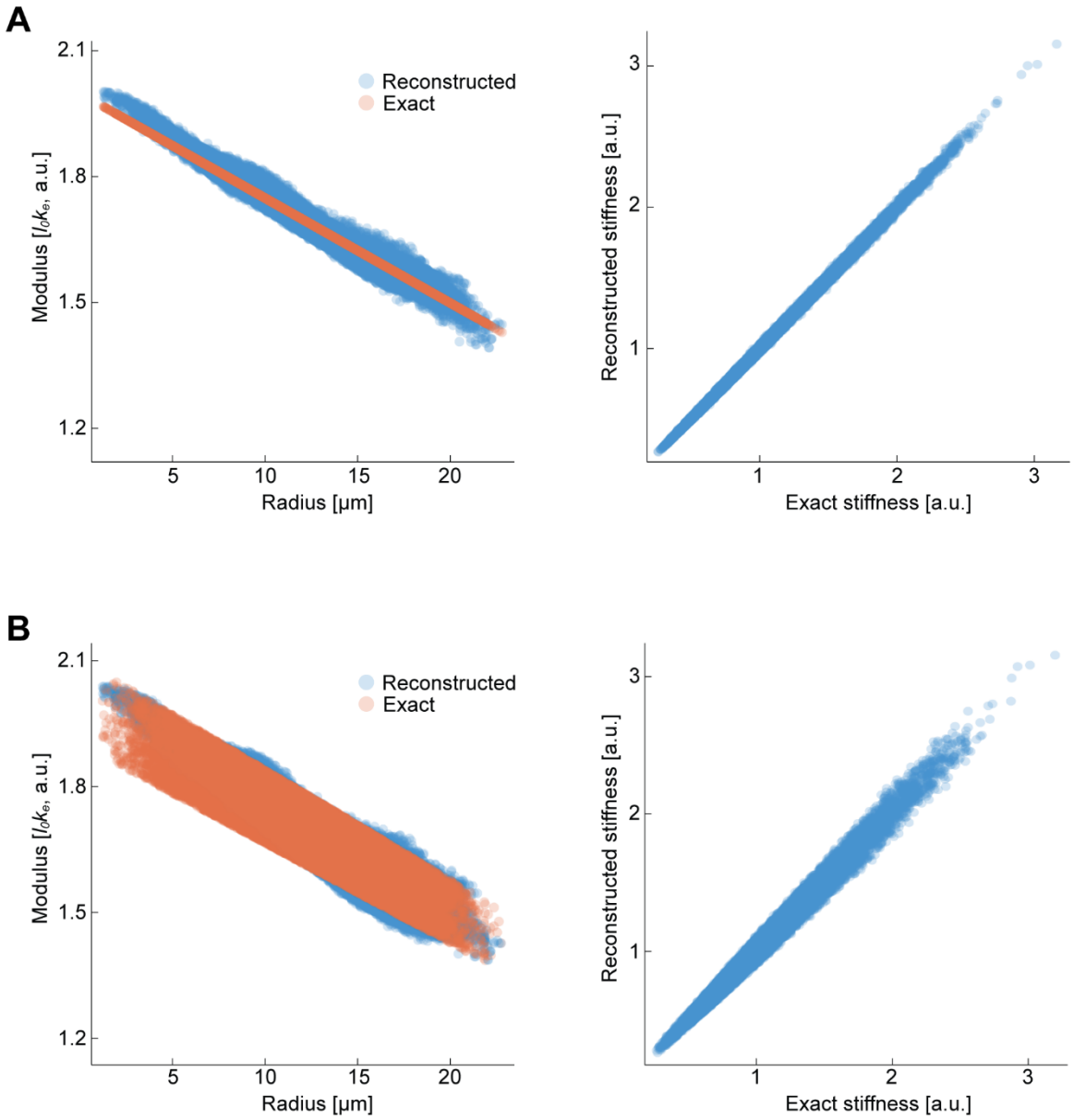

Figure S10: Mechanical inference on simulated data recovers true spring stiffnesses.
A) For biofilms with a simulated elastic modulus $l_0 k_e$ that decreases linearly with radial position in the biofilm, the mechanical inference recovers the spring stiffnesses k_e almost exactly (right), and it recovers the trend in modulus (left). We searched over the first *n* = 50 eigenvectors of the Laplacian, and due to this regularization, we do not expect perfect reconstruction. B) After randomly scaling the spring stiffnesses in the simulated biofilm, k_e, by a uniformly distributed amount between -5% and 5%, the mechanical inference still recovers back the stiffnesses (right) and the general trend of moduli with radius (left). Again, the first *n* = 50 eigenvectors of the Laplacian were used for the inference.

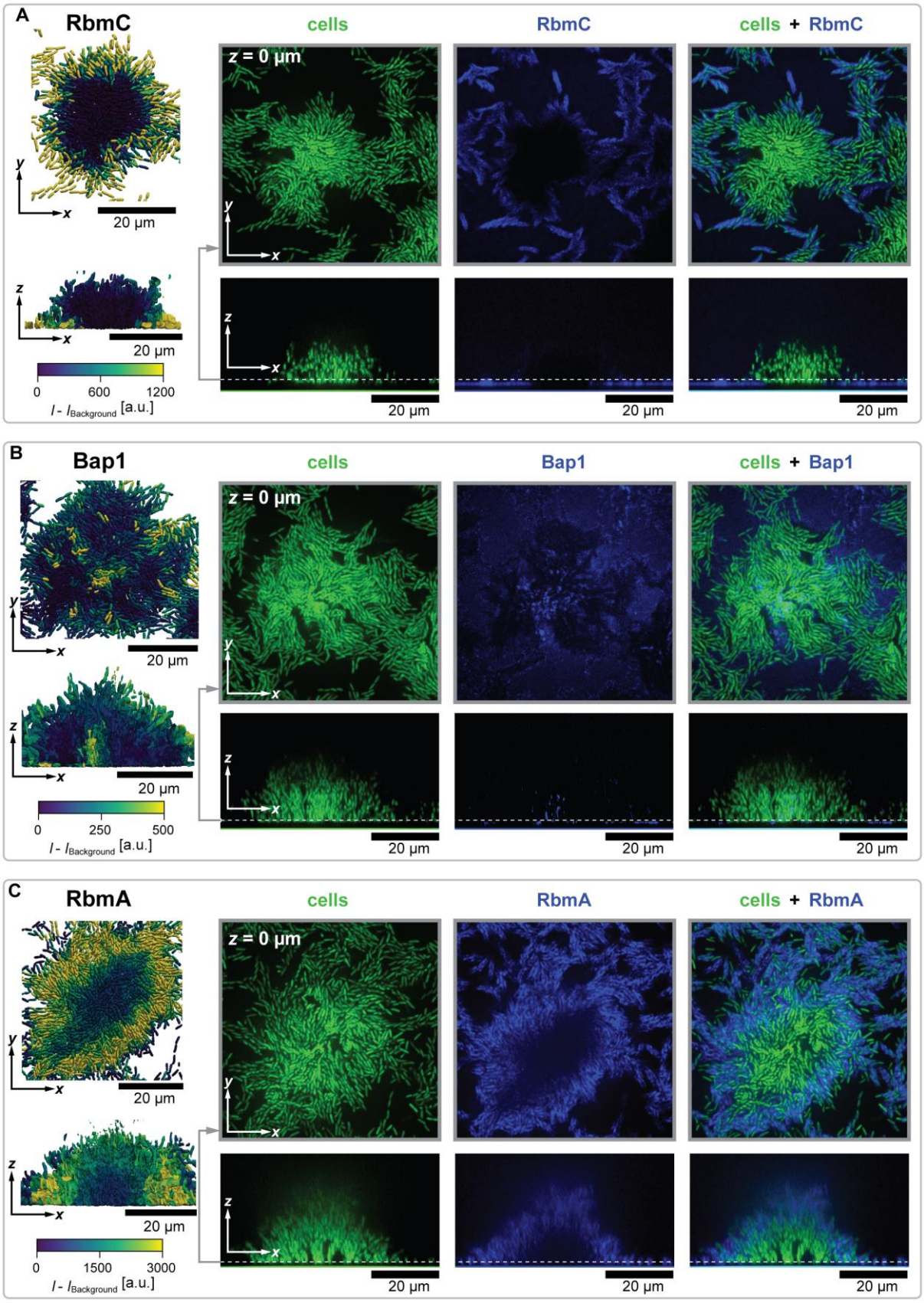

Figure S11: Distribution of extracellular matrix proteins RbmC, Bap1, RbmA in *V. cholerae* biofilms. A) Projections of 3D visualizations of biofilms (left top: *xy*-view, left bottom: *xz*-view), where each cell is colored by the mean concentration of the extracellular matrix protein RbmC around it. RbmC levels were measured by detecting RbmC-FLAG using an anti-FLAG antibody conjugated to Alexa Fluor 647.

Raw images in the *xy*-plane and *xz*-plane are shown for cells (green), immunofluorescence-labelled matrix protein RbmC (blue), and overlaid images. B) 3D distribution of the matrix protein Bap1 in biofilms, using an analogous presentation to panel A. Bap1 levels were measured by detecting Bap1-FLAG using an anti-FLAG antibody conjugated to Alexa Fluor 647. C) 3D distribution of the matrix protein RbmA in biofilms, using an analogous presentation to panel A. RbmA levels were measured by detecting RbmA-His using an anti-His antibody conjugated to Alexa Fluor 647.

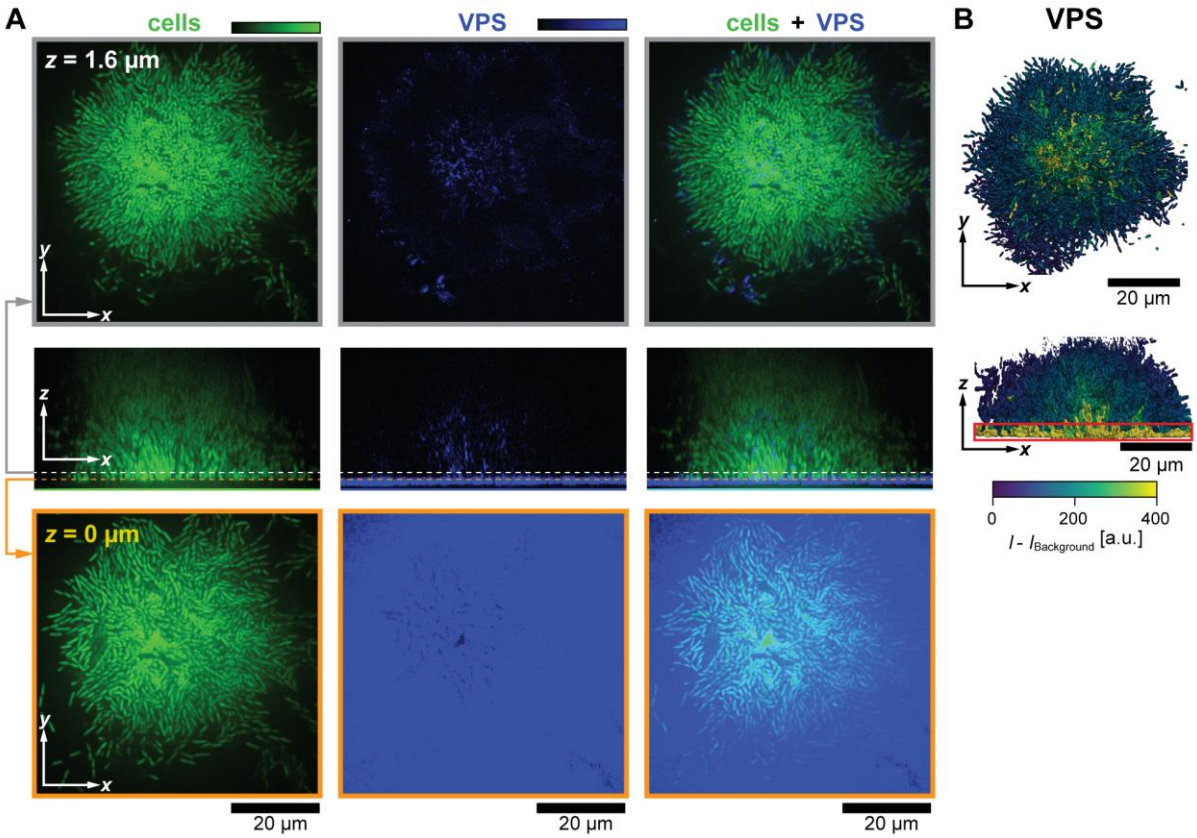

Figure S12: Distribution of extracellular matrix polysaccharide VPS in *V. cholerae* biofilms.
A) Raw images in the *xy*-plane and *xz*-plane are shown for cells (green), extracellular matrix polysaccharide VPS (blue), and overlaid images. VPS levels were measured by detecting lectins (WGA and Concanavalin A) conjugated to Alexa Fluor 633. Raw *xy*-images are shown at different *z*-positions: z = 1.6 µm and z = 0 µm. The raw images at z = 0 µm show that the lectins display a very high signal close to the glass surface, irrespective of the presence of a biofilm or individual surface-attached cells. Just above the surface, at z = 1.6 µm, the lectin signal is more specific to the biofilm. Raw images are shown using the same color range. B) Projections of 3D visualizations of biofilms (left top: *xy*-view, left bottom: *xz*-view), where each cell is colored by the mean concentration of VPS around it. The cells near the bottom of the biofilms have an elevated level of VPS around them, due to the high lectin levels on the glass surface – these cells near the bottom of the biofilm are indicated by a red box in the *xz*-projection of the 3D visualization.

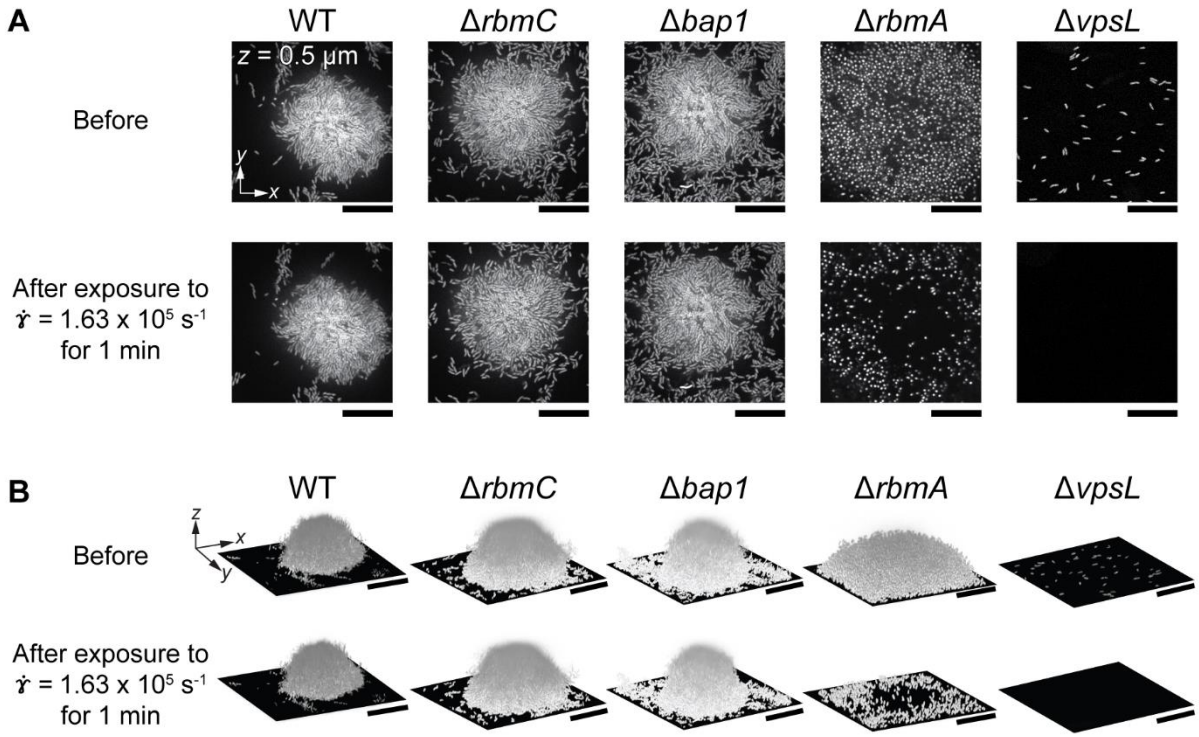

Figure S13: Biofilms of *V. cholerae* mutants lacking individual extracellular matrix components display different resilience to fluid shear.

A) Microscopy images of the *xy*-plane at *z* = 0.5 µm above the glass surface bottom, for the *V. cholerae* wild type (WT) and mutants lacking RbmC (Δ*rbmC*), Bap1 (Δ*bap1*), RbmA (Δ*rbmA*), or VPS (Δ*vpsL*). For each strain, images were acquired at a shear rate of $\dot{\gamma} = 0$ s^{-1}, immediately before the shear rate was increased to $\dot{\gamma} = 1.63$ x 10^5 s^{-1} for 1 min, and images were acquired after exposure to this high shear rate. Scale bars are 20 µm. The WT, Δ*rbmC*, and Δ*bap1* strains display biofilms with similar resilience to fluid shear. The Δ*rbmA* biofilms are ripped off the fluid shear, yet some individual cells remain attached to the glass surface. The Δ*vpsL* strain does not develop 3D biofilms, and the strong shear rate rips of even the individually attached cells. B) 3D biofilm morphologies of *V. cholerae* WT and mutants with deletions of individual extracellular matrix components, before and after exposure to a shear rate of $\dot{\gamma} = 1.63 \times 10^5$ s^{-1} for 1 min. Scale bar is 20 µm.

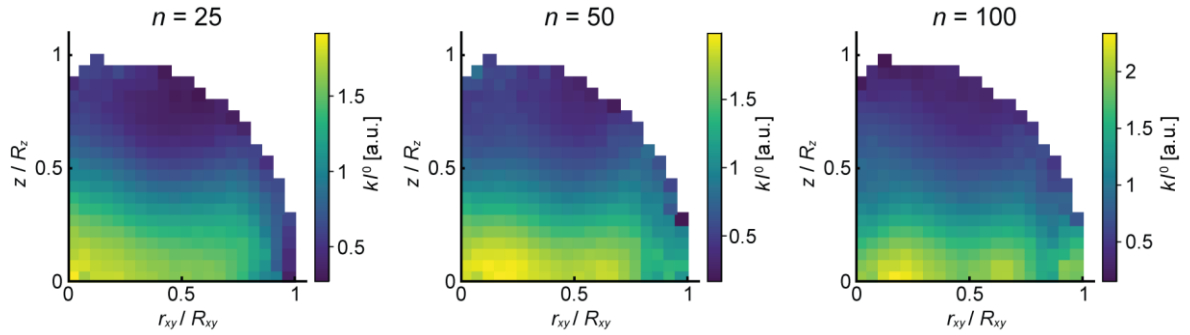

Figure S14 The number of Laplace modes does not qualitatively affect the inference of the spatial distribution of spring stiffnesses.

Reconstructing the spatial distribution of the average spring modulus for n = 25, 50, 100 Laplace modes recovers the same qualitative inference pattern: a stiff biofilm core and a stiff region near $\frac{r_{xy}}{R_{xy}} = 1, \frac{z}{R_z} = 0$. Using fewer Laplace modes constrains the resulting inference to be more spatially continuous. Increasing the number of Laplace modes allows for sharper gradients in the spring modulus. This can be seen in the locally higher stiffnesses in the core for n = 100 modes as compared to *n* = 25. Since

increasing or decreasing the mode number by a factor of 2 does not qualitatively change the mechanical pattern, we conclude that our inference is robust to this parameter.

Table S1: *V. cholerae* strains used in this study.

Strain	Genotype/ Relevant features	Reference
KDV613	N16961 *vpvC*^{W240R}, Δ*crvA* contains plasmid pNUT542	Hartmann, et al., Nat. Phys., 2019
KDV692	N16961 *vpvC*^{W240R}, Δ*rbmA* contains plasmid pNUT542	Hartmann, et al., Nat. Phys., 2019
KDV1412	N16961 *vpvC*^{W240R}, Δ*rbmC* contains plasmid pNUT542	
KDV1414	N16961 *vpvC*^{W240R}, Δ*bap1* contains plasmid pNUT542	
KDV1491	N16961 *vpvC*^{W240R}, Δ*crvA* contains plasmid pNUT542, rbmC-3xFLAG	
KDV1625	N16961 *vpvC*^{W240R}, Δ*crvA* contains plasmid pNUT542, bap1-3xFLAG	
KDV1663	N16961 *vpvC*^{W240R}, Δ*crvA* contains plasmid pNUT542, rbmA-His	
KDV1890	N16961 *vpvC*^{W240R}, Δ*vpsL* pTac_double sfgfP was inserted at lacZ site	
KDV2013	N16961 *vpvC*^{W240R}, Δ*crvA* contains plasmid pNUT1029	This work

Captions of Videos:

Video S1

Visualization of *V. cholerae* biofilm deformation during exposure to an increase in shear rate from 0 to 4.08 x 10^4 s^{-1}, followed by a reduction back to 0 s^{-1}. This video contains 81 time points, and at each time point we acquired a full confocal 3D image with 400 nm *z*-spacing. At each imaging time point, the shear rate was constant. However, between each imaging time point, the shear rate was increased or decreased: between time points 1 – 41, the shear rate was increased by increments of 0.102 x 10^4 s^{-1} from 0 to 4.08 x 10^4 s^{-1}; between time points 41 – 81, the shear rate was decreased by increments of 0.102 x 10^4 s^{-1} from 4.08 x 10^4 to 0 s^{-1}. To reduce photo-exposure and photo-damage as much as possible, we generated a high fluorescence signal from the cells by adding a DNA-binding dye (Syto 9 Green Fluorescent Nucleic Acid Stain, 5 µmol/l, Sigma) to the inflowing M9 medium.

Acquiring 3D images at many time points during the biofilm deformation enables us to track cells easier. However, we noticed that prolonged exposure to the DNA-binding dye caused a substantial softening of the biofilm, which prohibited the regular use of this technique for characterizing mechanical properties of biofilms.

Video S2

This video visualizes the flow around a *V. cholerae* biofilm colony in a microfluidic channel using 0.1 µm fluorescent tracer beads. The different picture frames of the video correspond to different *z*-heights in the channel (the *z*-position is indicated at the top left). Each picture frame of the video shows, for a particular *z*-position in the channel, the raw fluorescence image of the tracer beads (left), the raw fluorescence image of the biofilm with the flow field vectors overlaid (center), and the flow speed around the biofilm (right).